JGR Earth Surface

RESEARCH ARTICLE
10.1029/2025JF008352

Evolution of Shear-Zone Fractures Presages the Disintegration of Thwaites Eastern Ice Shelf

Debangshu Banerjee[1], David A. Lilien[2], Martin Truffer[3], Adrian Luckman[4], Christian T. Wild[5], Erin C. Pettit[6], Ted A. Scambos[7], Atsuhiro Muto[8], and Karen E. Alley[1]

[1]Department of Environment and Geography, Centre for Earth Observation Science, University of Manitoba, Winnipeg, MB, Canada, [2]Department of Earth and Atmospheric Sciences, Indiana University, Bloomington, IN, USA, [3]Geophysical Institute and Department of Physics, University of Alaska Fairbanks, Fairbanks, AK, USA, [4]Department of Geography, Swansea University, Swansea, UK, [5]Department of Geosciences, University of Tübingen, Tübingen, Germany, [6]College of Earth, Ocean, and Atmospheric Sciences, Oregon State University, Corvallis, OR, USA, [7]Earth Science and Observation Center, CIRES, University of Colorado Boulder, Boulder, CO, USA, [8]Department of Earth and Environmental Science, Temple University, Philadelphia, PA, USA

Abstract Thwaites Eastern Ice Shelf (TEIS) is a partially confined floating extension of Thwaites Glacier, anchored by an offshore pinning point at its northern terminus. Over the past two decades, the shelf has experienced progressive fracturing around a prominent shear zone upstream of its pinning point, gradually compromising its structural integrity. Here we present an analysis of shear-zone fracture evolution from 2002 to 2022 and its control on the flow dynamics of the ice shelf using satellite remote sensing and in situ GPS observations. We compiled multi-year statistics of fracture length and orientation from Landsat and Sentinel-1 imagery and compared their changes with evolving flow dynamics and surface strain rates. Ongoing disintegration driven by the shelf's shearing against the pinning point occurred in two stages: propagation of large shearing fractures approximately parallel to flow earlier in the record, followed by the rapid formation of smaller tensile fractures approximately perpendicular to flow later in the record. We also observed velocity perturbations originating from the shear zone and propagating across the main ice shelf, observationally demonstrating the direct impact that shear-zone disintegration has on the dynamics of TEIS.

Plain Language Summary Thwaites Glacier, a key outlet of the West Antarctic Ice Sheet, is losing ice rapidly. Uncertainty in the future behavior of Thwaites Glacier constitutes one of the major uncertainties in global sea level rise projections. Thwaites Eastern Ice Shelf is a floating extension of Thwaites Glacier and is anchored by a submerged ridge at its northern edge, called a pinning point. Pinning points obstruct the flow of the ice, also causing it to deform, compress, and fracture. Over the past 20 years (2002–2022), Thwaites Eastern Ice Shelf (TEIS) has experienced a significant increase in fracturing upstream of its pinning point. This area is termed a "shear-zone," due to the way that ice deforms in response. Using satellite imagery and GPS observations, we analyzed how fractures evolved in the last two decades and identified their link to changing ice-flow patterns. This yielded two key insights. First, fractures occurred in two stages: the initial propagation of long fractures parallel to ice flow, followed by smaller fractures perpendicular to ice flow. Second, we demonstrate that the shear-zone disintegration causes upstream ice-flow speed to increase on TEIS.

Key Points:

- Shearing of Thwaites Eastern Ice Shelf against its pinning point has been a major driver of its recent destabilization
- Shear-zone fracturing occurred in two phases: expansion of long shear fractures followed by an increase in the number of small tensile fractures
- Shear zone disintegration has a dynamic influence on regulating the upstream flow of the rest of the ice shelf

Supporting Information:

Supporting Information may be found in the online version of this article.

Correspondence to:

D. Banerjee,
banerjed@myumanitoba.ca

Citation:

Banerjee, D., Lilien, D. A., Truffer, M., Luckman, A., Wild, C. T., Pettit, E. C., et al. (2025). Evolution of shear-zone fractures presages the disintegration of Thwaites Eastern Ice Shelf. *Journal of Geophysical Research: Earth Surface*, *130*, e2025JF008352. https://doi.org/10.1029/2025JF008352

Received 24 MAR 2025
Accepted 7 AUG 2025

Author Contributions:

Conceptualization: Karen E. Alley
Data curation: Debangshu Banerjee, Martin Truffer, Adrian Luckman, Ted A. Scambos
Formal analysis: Debangshu Banerjee
Funding acquisition: Karen E. Alley
Investigation: Debangshu Banerjee
Methodology: Debangshu Banerjee, David A. Lilien, Karen E. Alley
Project administration: Karen E. Alley
Resources: Karen E. Alley
Software: Debangshu Banerjee
Supervision: Karen E. Alley
Validation: Karen E. Alley
Visualization: Debangshu Banerjee

1. Introduction

Thwaites Glacier in West Antarctica contains an estimated mass corresponding to 65 cm of global sea-level rise (Morlighem et al., 2020; Rignot et al., 2019) and is one of the fastest-changing ice-ocean systems in Antarctica (Scambos et al., 2017). Experiments by Seroussi et al. (2017) suggest that Thwaites Glacier will experience grounding-line retreat at a rate of 1 km yr^{-1}, along with flow acceleration over the next four decades. This dynamic response is projected to lead to increased mass loss at an average rate of 1.2–1.6 Gt yr^{-2}, corresponding to an annual contribution to sea-level rise of approximately 0.21–0.29 mm yr^{-1}. Much of the ice sheet within the catchment of Thwaites Glacier is grounded on a retrograde bed, a configuration that makes it susceptible to dynamic instability and irreversible retreat (Schoof, 2007a, 2007b). Some observational and modeling evidence suggests that such a retreat is already underway (Joughin et al., 2014; Milillo et al., 2022; Reese et al., 2023; Rignot et al., 2014). By contrast, Hill et al. (2023) suggest that there is no indication of a marine ice sheet instability in the current state. However, Thwaites Glacier continues to retreat despite suppressed basal melting at

Writing – original draft: Debangshu Banerjee
Writing – review & editing: Debangshu Banerjee, David A. Lilien, Martin Truffer, Adrian Luckman, Christian T. Wild, Erin C. Pettit, Ted A. Scambos, Atsuhiro Muto, Karen E. Alley

its grounding zone (Davis et al., 2023; Schmidt et al., 2023) because of an insulating layer near the ice-ocean interface (Dotto et al., 2022) that likely extends far underneath the Eastern Ice Shelf (Wild et al., 2024).

Thwaites Glacier has two distinct floating sections: the Thwaites Western Ice Tongue (TWIT), an unconfined fast-flowing ice tongue fed by the main trunk of Thwaites Glacier; and the Thwaites Eastern Ice Shelf (TEIS), a partially confined ice shelf toward the east (Alley, Wild, et al., 2021; Wild et al., 2022) that rests on an offshore pinning point at its northern terminus (Wild et al., 2022). For the last two decades, this pinning point has played a crucial role in regulating the shelf's flow dynamics (Alley, Wild, et al., 2021). The pinning point consisted of a single ice rumple, but persistent thinning of the ice shelf led to the formation of a larger, less grounded eastern portion and a smaller, more grounded western portion (Figure 1). Continued weakening caused both ice rumples to gradually lose their anchoring, allowing ice to flow between them over a saddle in the underlying bathymetric ridge (Wild et al., 2022).

TEIS and TWIT shared a common shear margin, which maintained its structural integrity until 2006–2007 (Alley, Wild, et al., 2021; Wild et al., 2022). After 2002, with the acceleration of TWIT, the robust and intact TEIS/TWIT shear margin dragged TEIS forward (Alley, Wild, et al., 2021). The shear margin began to disintegrate around the end of 2007, progressively disconnecting the ice shelf from its western portion by 2009. As a result, TEIS decelerated once the shearing stresses from TWIT were alleviated (Wild et al., 2022). After the TEIS/TWIT shear-margin breakup, TEIS has undergone a progressive fracturing and disruption over the last decade (Alley, Wild, et al., 2021), marked by the penetration of extensive rifts and crevasses across much of its width upstream of the pinning point (Alley, Wild, et al., 2021; Benn et al., 2022; Wild et al., 2022). In the region just south of the pinning point, a more complex evolution has occurred. We refer to this fractured region as a pinning-point "shear zone" (Figure 1). The shear zone fractures expanded in response to the shelf's accelerated movement from 2002 to 2006 and gained further prominence after the TWIT/TEIS shear-margin breakup in response to increased shear strain. Wåhlin et al. (2021) proposed that direct basal melt may also contribute to fracture in the shear zone by thinning of the ice, thus making it more susceptible to fracturing under stress (Benn et al., 2022). Overall, progressive weakening of the shear zone resulted in a rapid and ongoing acceleration of the upstream ice shelf, with frequent calving episodes at the eastern and western flanks (Benn et al., 2022). This led to the gradual weakening of the shelf's pinning-point buttressing (Wild et al., 2022). With the expansion of fractures, as the connection to the pinning point is lost, the remaining buttressing provided by the ice shelf shifts toward small embayments distributed along the complex grounding zone (Gudmundsson et al., 2023; Wang et al., 2025; Wild et al., 2022).

Alley, Wild, et al. (2021) provided a comprehensive overview of the dynamic changes occurring on TEIS over the last two decades leading to the shelf's progressive destabilization. They argued that three mechanisms could cause complete collapse of TEIS in the coming years. One of these was the decoupling of the shelf from the pinning point due to large-scale failures occurring in the shear zone. Benn et al. (2022) also mentioned that continued strain concentration and rift formation have ensured that the ice in the shear zone has remained the "weakest link in the system." In this study, we present an assessment of the evolution of the shear zone upstream of the pinning point in the last two decades and analyze how this evolution has affected the overall flow dynamics of the shelf using satellite remote sensing and in situ GPS observations. Our investigation highlights a chronology of fracture evolution within the shear zone and investigates the processes driving this evolution from 2002 to 2022. We also demonstrate how this evolution of shear-zone fractures has progressively affected the overall flow dynamics of TEIS in the last two decades.

2. Materials and Methods

2.1. Delineation of Study Sub-Regions

First, we analyzed the fracture evolution pattern in the shear zone upstream of the pinning point to understand the disintegration pattern of the shelf. To quantify the growth of fractures on TEIS, we outlined three areas of interest (AOI) within TEIS (Figure 1): the pinning-point shear zone (marked in dashed and dotted blue), the mid-shelf region (marked in dashed black), and the region upstream of the pinning point (marked in dotted red; Figure 1). These AOIs do not advect with the flow. We have adhered to an Eulerian framework for this analysis, primarily because these regions are defined relative to the pinning point, which remains fixed in space. We determined the shear-zone boundaries on two criteria: the extent of migration of fractures upstream of the pinning point from 2002 to 2022 and the shelf's changing width within the two decades. We selected the mid-shelf region to encompass a significant amount of TEIS's central ice mass while including only intact ice in between the

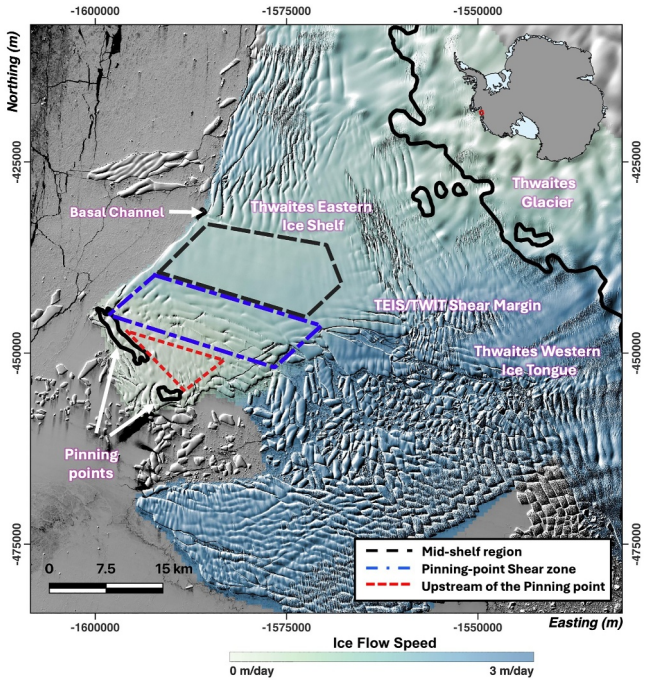

Figure 1. Study area: Thwaites Eastern Ice Shelf (TEIS) and surroundings. TEIS, Thwaites Western Ice Tongue (TWIT), pinning points, shear margin between TEIS and the TWIT, and Thwaites Glacier are also labeled, terms discussed in the text. Three sites of interest are indicated using three different polygons: the pinning point shear zone (blue dotted and dashed line), mid-shelf region (black dashed), and region upstream of the pinning point (red dotted). The grounding lines (black solid lines) are from Wild et al. (2022). The background image (EPSG 3031) is from a Landsat panchromatic image captured in December 2014, and the flow speed is from the ITS_LIVE velocity in 2014.

upstream boundary of the shear zone and a basal channel on the shelf's eastern boundary (described in Alley et al. (2024)). Finally, we defined the region upstream of the pinning point as the area between the downstream boundary of the shear zone and the extent of the pinning point, as marked by Wild et al. (2022).

2.2. Fracture and Internal Mélange Depiction From Satellite Images

We manually digitized and mapped two categories of surface features within the shear zone, visible in satellite images from 2000 to 2022: "fractures" and "internal mélange areas." We defined fractures as the cracks in the ice shelf surface visible as single lines and surface depressions as an expression of basal crevasses. Internal mélange areas are discrete open regions within the ice shelf that developed from full-thickness rifts and are typically filled with ice mélange. We digitized mélange using the polygons in GIS (Figure S4 in Supporting Information S1).

We delineated surface fractures and internal mélange areas using high-resolution (15 m) panchromatic bands from Landsat 7, 8, and 9 spanning from 2002 to 2022. We selected one Landsat image per austral summer (September–March), capitalizing on the minimal cloud cover ranging from 0% to 5%. Unfortunately, no cloud-free Landsat images were available in the Austral summer of 2005–2006. Each image was radiometrically scaled appropriately to enhance visibility that help us delineate the fractures clearly. We also used Sentinel-1 SAR images to track surface fractures and mélange areas at monthly resolution from January 2020 to July 2022, corresponding to the time when AMIGOS GPS observations were collected. Higher-resolution Sentinel-1 SAR observations during this time period allowed us to analyze changes observed in the GPS record on short timescales. For the Sentinel-1 imagery, we maintained a minimum 20-day gap between two consecutive images. Prior to analysis, we preprocessed all the SAR images in SNAP v10.0 software using Sentinel-1 preprocessing tools. These include thermal and border noise removal, radiometric calibration, speckle filtering, and geometric terrain correction to enhance clarity and improve tracking of the fractures.

For our analysis, a fracture is defined as a visually continuous linear or curvilinear crack visible in imagery. These cracks were digitized using polylines in GIS. In cases where two cracks intersect or form an orthogonal connection, they are counted as separate fractures as they exhibit distinguishable propagation directions or orientations (Figure S4 in Supporting Information S1). The edges of ice mélange areas are considered as fractures for digitization, and to avoid the double-counting of the fracture length arising from both sides of an internal mélange, we excluded one side while calculating the total and average length as well as the orientations of the fractures. The side of a mélange feature selected for inclusion was determined based on fracture digitized from the earlier time series of satellite imagery (Figure S4 in Supporting Information S1). Each internal mélange structure originated and expanded from a parent fracture. We consistently digitized the mélange edge that was closely aligned with the position of its parent fracture. This approach allowed us to preserve the temporal continuity of individual fracture features across subsequent years. While digitizing mélange, we have also excluded mélange outside the western boundary of the shelf, even if it falls within the shear zone boundary, since it lies outside the shelf and is unlikely to alter ice dynamics.

After tracing the fractures and mélange in the satellite images, we produced a time series of total and average fracture length and mélange area annually from 2002 to 2022 and monthly from January 2020 to July 2022. Additionally, we examined the changing orientations of the fractures. For all the total length and orientation calculations, we applied a minimum threshold of 500 m for fracture length, ensuring the elimination of smaller digitization errors. We measured the orientations of the fractures assuming a straight-line angle between the origin and the tip of each fracture clockwise from grid north (0°) in the EPSG 3031 projection. Finally, since fractures extend in two opposite directions, we took modulo 180 of each value. A few curvilinear features were identified

toward the eastern flank near the pinning point, and their orientations were calculated using the same method. These features have a small curvature and are relatively few in number compared to the total number of fractures. Therefore, they do not significantly affect the overall fracture statistics.

Errors in manual digitization could arise from various sources, including the visual misidentification of fractures, poor visibility of crevasses in satellite images, geometric inaccuracies, and variations in the radiometric and spectral resolutions of Landsat 7, 8 and 9. The visibility of fractures in Sentinel-1 SAR images can be affected by the variation in dielectric properties of the surface subjected to changes in the firn moisture content. To address this issue of digitization errors, we conducted a comparative analysis using coincident Landsat and Sentinel-1 imagery from early and late summer periods of 2021. Since Landsat images are not affected by dielectric changes, it served as a reference to assess visibility-related differences in Sentinel-1. We computed the difference in total and average fracture lengths between the two sensors for both time periods. Then, from these estimates, we calculated the absolute difference between these variations in lengths to estimate the error attributed to seasonal changes in fracture visibility in Sentinel-1. This yielded a visibility-induced error of ±0.35 km for average fracture length and ±6.28 km for total fracture length. Our error bars in Figures 2 and 5 account for this visibility-induced error as well as the digitization error discussed below.

To quantify the digitization errors, we re-digitized fractures and mélange from 5 selected image sources in 2021, 2014, 2010, 2007, and 2002 from Landsat 7, 8, and 9 (Figure S5 in Supporting Information S1). We re-digitized one Sentinel-1 image every 6 months (January and July of 2020, 2021, and 2022) from the selected time period. We then calculated the mean relative differences between the digitized and the re-digitized fractures' length and mélange areas and applied the average over all the data sets. This process revealed an average error of ±3.9% for total fracture length and ±2.8% for average fracture length from Landsat. For Sentinel-1, we found an error of ±4.6% for total fracture lengths and ±3.3% for average fracture lengths in Sentinel-1. For internal mélange areas, the average errors are ±15.4% for Landsat images and ±9.5% for Sentinel-1 images. Notably, the highest errors were found between 2007 and 2012, attributable to the scan-line errors in Landsat 7, introduced on 31 May 2003, which particularly affected the measurement of short-length fractures on the shelf's eastern and western margins.

We also assessed digitization error distribution across different fracture length categories. We grouped fractures into five bins based on their lengths: ≤2, 2.01–4, 4.01–6, 6.01–8, and >8 km. For each bin, we computed the mean relative differences between the original and re-digitized fractures across six sampled years (2002, 2006, 2010, 2014, 2018, and 2021). The evaluation was done in terms of both total fracture length and average fracture length within each category. The results show that relative differences in total and average fracture length are particularly high in the shortest (<2 km) and longest (>8 km) fracture categories (Table S2 in Supporting Information S1). Higher errors in the short-fracture category highlight challenges in consistently detecting small features across yearly digitizations, especially in dense fracture areas. The higher average-length error in the shortest bin (20.99%) also underscores the similar difficulties in accurately delineating small fractures, especially when they are visually ambiguous. The higher error in the >8 km category may stem from inconsistent tracing of long fractures, considering that this range can encompass very long lengths. In contrast, the three intermediate length categories exhibit generally low relative differences, suggesting improved consistency in digitization practices for fractures of moderate scale.

2.3. Remotely Sensed Ice-Flow Dynamics

We compiled three satellite velocity products for this investigation. Details of these products have been mentioned in Table S1 in Supporting Information S1. From 2002 to 2013, we used the velocity and strain-rate averages over TEIS (spatial resolution 500 m) computed by Alley, Wild, et al. (2021) using cross-correlation between MODIS and Landsat images. From 2013 onwards, we utilized the ITS_LIVE image-pair global ice velocities (Gardner et al., 2019), which are available at higher spatial resolution (120 m) and temporal resolution. The ITS_LIVE velocity composites were prepared from Landsat-8, Landsat-9, Sentinel 2, and Sentinel 1 satellite images implementing the AutoRIFT feature-tracking algorithm (Lei et al., 2021). We prepared annual velocity composites for 2013–2022 using ITS_LIVE image-pair velocities available throughout a year, keeping the extent and the spatial resolution the same for every annual composite. Each annual composite was calculated by stacking all available image pairs and taking the median value of the stack of values at each grid cell. Some small data gaps persisted in the velocity record closer to the grounding line, which were filled using bilinear interpolation.

Monthly velocity composites were produced from January 2016 to December 2022 using speckle tracking from image pairs of Sentinel-1 Interferometric Wide Swath (IW) mode. Before December 2021, when Sentinel 1A and 1B were active, velocity maps were generated from image pairs from Sentinel 1A and Sentinel 1B available at 6- and 12-day intervals. For each month, up to 10 velocity files were averaged to create a monthly velocity composite. After the Sentinel-1B mission ended in December 2021, at most two measurements were averaged since only 12-day pairs were available from Sentinel 1A. Consequently, the data sets after December 2021 are noisier and have larger data gaps. We employed standard feature/speckle tracking procedures (Luckman et al., 2015) to generate these velocity fields. The feature tracking window size was set to 416 × 128 pixels, which equates to ∼1 km in range and azimuth. We sampled the velocity field at 50 × 10 pixels before geocoding to the Antarctic Polar Stereographic projection (EPSG:3031) at 100 m resolution using the REMA mosaic DEM (Howat et al., 2019) for geometric correction; DEM gaps were filled using Bedmap2 surface topography data (Fretwell et al., 2013).

Next, we computed the surface strain rates (in flow-coordinates) from the remotely sensed velocity records over a length-scale of 3 km using a logarithmic strain-rate formulation (Nye, 1959) that relies on a numerical stake-tracking scheme developed by Alley et al. (2018). The overall results produced a 20-year record of longitudinal, transverse, and shear strain rates on TEIS. We also computed the average flow speed and direction from the velocity components as well as ice flow divergence (a combination of longitudinal and transverse strain rates) from the strain rate components.

Uncertainty in velocity estimation stems from the errors in the geolocation accuracy of the satellite images (Wolfe et al., 2002) and the cross-correlation of pixels between satellite images (Fahnestock et al., 2016). Alley, Wild, et al. (2021) reported a maximum error of ∼450 m yr^{-1} for individual MODIS image pairs over ice shelves flowing at ∼750 m yr^{-1}. However, our analysis uses the annual composite product from the same study, which offers significantly improved accuracy. Similarly, the errors in individual Sentinel-1- derived velocities are estimated to be less than 100 m yr−1 (Luckman et al., 2015). For ITS_LIVE, velocity products are generated from Landsat and Sentinel-1 images. These images have variable error estimates based on several factors, including surface texture and contrast, image registration accuracy, cloud cover, radiometric noise, temporal baseline, and time intervals between images. Gardner et al. (2019) provide detailed information on the error estimation method and errors for different satellite estimates. The products provide horizontal error estimate components associated with each image. From those, we estimated the maximum error of 350 m yr^{-1} for ITS_LIVE composites.

We utilized the computed strain rates and flow-divergence parameters to generate time series for the three AOI within TEIS. For example, we compared the changes in fracture length and internal mélange area with the temporal variations in average shear strain rates (shearing) and flow divergence within the shear zone to gain insights into the shear-zone fracture dynamics. Additionally, we developed a time-series of total longitudinal strain rates over the mid-shelf and upstream of the pinning point to better understand how the evolution of shear-zone fractures affects ice-shelf flow dynamics. Based on the series of events that occurred in TEIS during the last two decades (Alley, Wild, et al., 2021), we have divided the entire study period into four distinct phases for both analytical convenience and ease of comparison: 2002–2006 (Phase 1: TWIT-driven acceleration period), 2007–2011 (Phase 2: TEIS/TWIT shear-margin disintegration period), 2012–2016 (Phase 3: TWIT disintegration period), and 2017–2022 (Phase 4: mid-shelf acceleration period of TEIS). These phases are visually represented in Figures 2a–2c using four vertical color patches.

2.4. AMIGOS In Situ Ice-Flow Speed Measurements

In early 2020, two Automated Meteorology-Ice-Geophysics Observation Systems (AMIGOS) stations (Scambos et al., 2013, 2025) were installed on TEIS as part of the Thwaites-Amundsen Regional Survey and Network project of the International Thwaites Glacier Collaboration (ITGC). These stations were equipped with automated GNSS receivers, which tracked their movement through their observational lives, which concluded in mid-2022. Dual-frequency GPS data were collected using an integrated Topcon GRS-1 receiver with a PGA-1 antenna, recorded at 30-s intervals during three to five 20-min sessions daily.

We processed the data set against Polenet stations on Thurston Island, Bear Peninsula, and Backer Island using the track processing module of MIT's GAMIT/GLOBK software (Herring et al., 2008). Multiple base stations were used to address incomplete records at a single station. The resulting positions were converted to the Antarctic

Polar Stereographic projection (EPSG:3031) with the transformer class from Python's pyproj library (Whitaker et al., 2019). After conversion, the data were cleaned to remove outliers. We used the variations exceeding 3 m from a second-order fit of time versus each coordinate. After that, the data were transformed into an along-flow and across-flow coordinate system. Finally, the records were interpolated to 15 min intervals using the Scipy library (Virtanen et al., 2020) and speeds were calculated by smoothing the along-flow component with a lowess filter from the nonparametric package of Python's statsmodels library (Seabold & Perktold, 2010). The AMIGOS GPS observations provide ice-flow speed data at much higher precision and temporal resolution than satellite-derived products. Here, we only consider the record from the Cavity Camp AMIGOS station. The observation is available from early 2020 to mid 2022 (Truffer et al., 2025). To ensure that the observed signal in the GPS data was due to a temporal change in the state of the ice shelf rather than a Lagrangian speed increase due to GPS advection into a faster flow regime, we corrected for spatial variability. This was done by subtracting the spatial trend in ice velocity derived from the ITS_LIVE long-term average Antarctic velocity grid (Gardner et al., 2019). Due to the small distance that the GPS traveled during the observation interval, this correction was very small, on the order of 1 cm/day.

3. Results

3.1. Progressive Evolution of Shear-Zone Fractures

The total annual length of fractures (blue line in Figure 2a) shows a significant increasing trend at the 95% confidence level over the past two decades. It increased from 165.2 ± 6.6 km in 2002 to 335.5 ± 13.4 km in 2021. From 2014, we observe a consistent increase in the total fracture length. We link this increase to the emergence of two large transverse rifts within the shear zone (visible in the December 2015 Landsat image), which propagated further toward the mid-shelf area in the subsequent years (explained in detail in Wild et al. (2024)). Their growth was accompanied by the emergence of new parallel rifts in the eastern sector. In addition, a population of pre-existing fractures gradually advected downstream into the shear-zone boundary, particularly along its western edge. Although their individual lengths remained unchanged, their movement into the shear-zone boundary resulted in an increase in the measured in situ fracture length.

On the other hand, the average length of fractures exhibited a declining trend. It reduced from 3.2 ± 0.8 km in 2002 to 1.5 ± 0.2 km in 2021, which illustrates that, as time went on, the contribution of smaller fractures to the total fracture length gradually increased. During the TWIT-driven acceleration phase of 2005–2007, the average fracture length was predominantly high as longer fractures expanded within the shear zone. Post-2010, there was a marked reduction in the average fracture length as numerous smaller fractures emerged after the disintegration of the TEIS/TWIT shear margin. Post-2017, we observed another rapid decline in the average fracture length. The internal mélange area increased after 2010 (Figure 2b). However, from 2006 to 2009, no mélange was found within the shear zone. This observation contrasts with 2002–2005, when some mélange was present. The pre-existing mélange before 2006 was mostly concentrated around the eastern sector of the shear zone, which advected out of the shear zone during phase 1 (Figure S3 in Supporting Information S1). After 2010, new mélange began to form predominantly on the western side of the shear zone and steadily expanded eastwards in the subsequent years (Figure S3 in Supporting Information S1), reaching an area of 8.2 ± 1.3 km^2 by 2021. Notably, in 2022, there was a widespread increase in the mélange areas up to 16.5 ± 2.5 sq. km.

Substantial changes in average shear-strain rates and flow divergence occurred in and around the shear zone as fractures evolved with time. During the later part of the TWIT-driven acceleration phase, shearing and flow divergence in the shear zone were notably high (Figure 2c: blue patch). Following the shear-margin disintegration around 2008/09, these metrics declined sharply (Figure 2c: green patch). In the following years, from 2009 to 2017, shearing and flow divergence exhibited annual fluctuations. Commencing in 2017, an accelerating increase in both shearing and flow divergence was observed, aligning with the progressive fracturing and expansion of the mélange. Figure 3 illustrates spatial details of the progressive changes in high shear-strain rates and flow divergence closely aligned with shear-zone fractures, particularly after 2013, when ITS_LIVE velocity data were available (Figure 3a). After 2017, these metrics progressively intensified within the shear zone, and more and more surface fractures became visible.

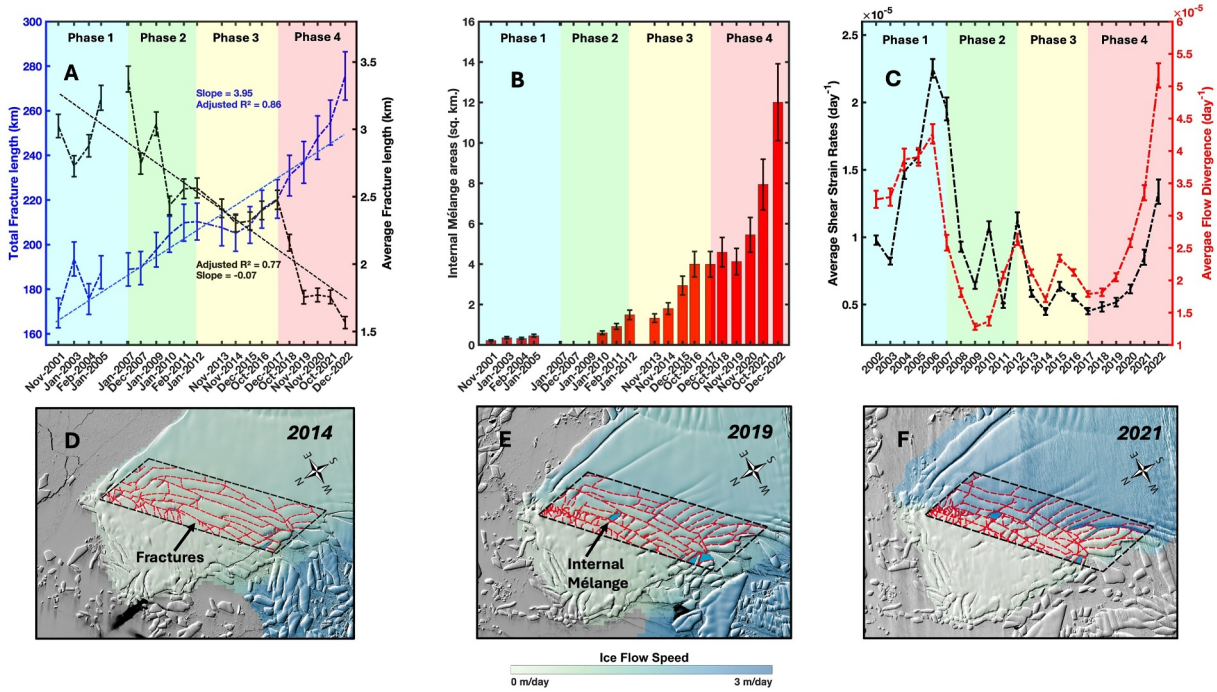

Figure 2. Changing fracture length and internal mélange area against shearing and ice flow-divergence. (a) Temporal changes in total fracture length (blue) and average fracture length (black) from 2002 to 2022. The blue and black dotted lines show the trend in total and average fracture lengths, respectively (significant at a 95% confidence level) (b) Evolution of internal mélange areas from 2002 to 2022. The *x*-axis labels indicate the dates of the Landsat images used for digitizing fractures and mélange. (c) Variation in average shear strain rates and average flow divergence around the pinning-point shear zone from 2002 to 2022. (d–f) Digitized shear zone fractures in Thwaites Eastern Ice Shelf (TEIS) in 2014, 2018, and 2021, respectively, where the black dotted polygon shows the extent of the shear zone and red lines show the digitized fractures. The four patches in the background represent the four phases discussed in the text. Blue: Phase 1—TWIT-driven acceleration phase (2002–2006), Green: Phase 2—TEIS/Thwaites Western Ice Tongue (TWIT) shear margin breakup period (2007–2011), Yellow: Phase 3—TWIT disintegration phase (2012–2016) and Red: Phase 4—advanced mid-shelf acceleration phase of TEIS (2017–2022).

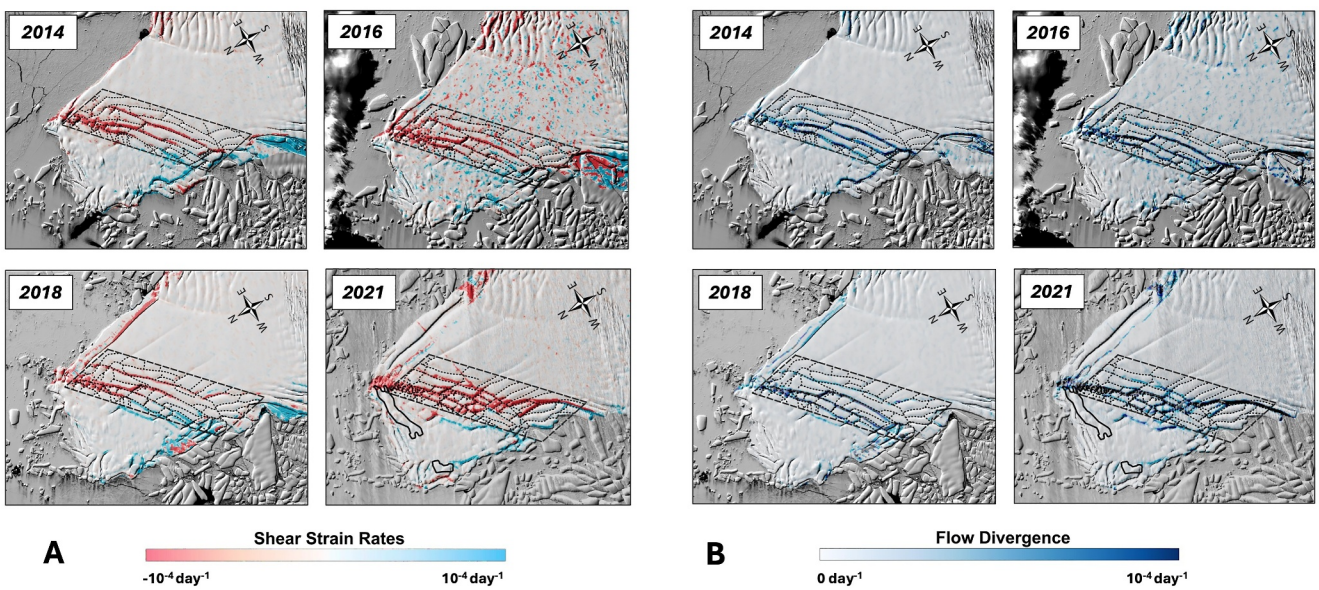

Figure 3. Changing shear-strain rates and flow divergence over Thwaites Eastern Ice Shelf (TEIS). (a) Shear-strain rates and (b) ice-flow divergence over TEIS in 2014, 2016, 2018, and 2021. For ice-flow divergence, only the positive values are shown. The background images include Landsat-7 and 8 panchromatic band images for the respective years used to digitize the fractures and mélange areas. In each plot, the black polygon indicates the extent of the shear zone throughout the study period. The black dotted lines represent the digitized fractures of the respective years overlaid on the maps.

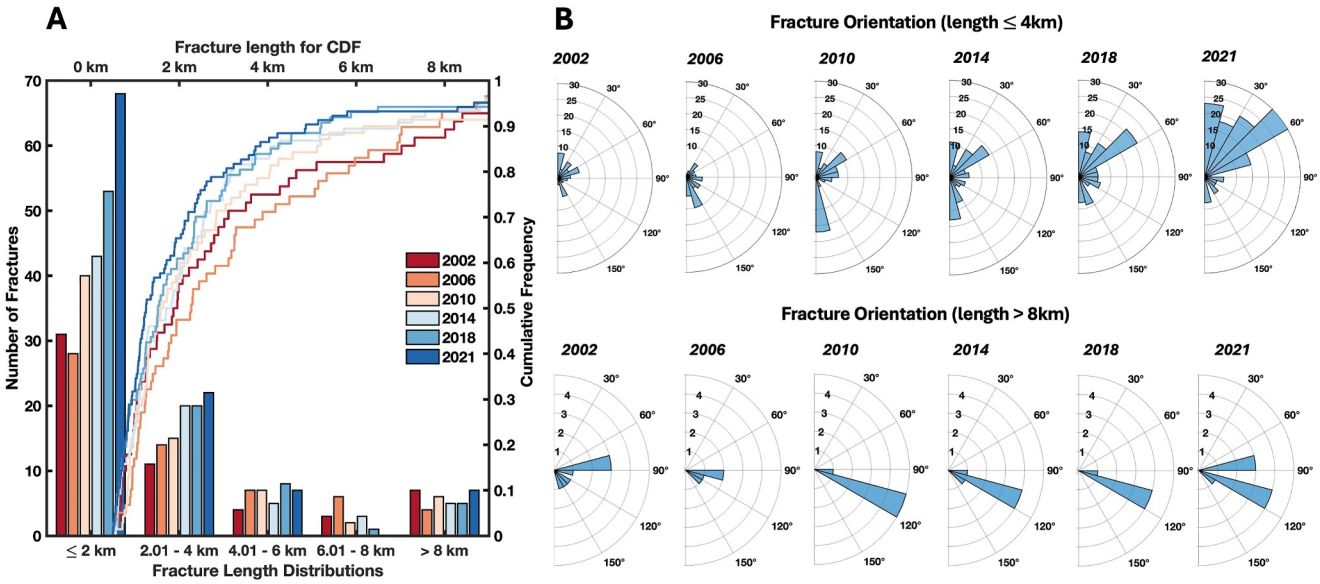

Figure 4. Changing distribution of shear-zone fractures' length and orientation. (a) Histograms and cumulative distribution function of pinning-point shear zone fracture lengths. (b) The upper panel illustrates the orientation of the shorter fractures (≤4 km), and the lower panel illustrates the orientation of the longer fractures (≥8 km). Angles are clockwise from grid north (0°) in the EPSG 3031 projection.

3.2. Evolving Configurations of the Shear-Zone Fractures

In the preceding section, we demonstrated that the average length of the fractures in the shear zone declined between 2001 and 2022, implying an increasing contribution from smaller-length fractures to the total fracture length as time progressed. To gain further insight, we analyzed the distribution of the fracture lengths and orientations in length bins of ≤2, 2.01–4, 4.01–6, 6.01–8, and >8 km (Figure 4). We chose six sampling years that capture the shear-zone dynamics during important events within the four phases, including the starting of TWIT-driven acceleration phase (2002), the advanced TWIT-driven acceleration phase (2006), the post-TWIT/TEIS-shear margin breakup (2010), the TWIT disintegration phase (2014), the starting of mid-shelf acceleration (2018), and finally the advanced mid-shelf acceleration (2021), but before the very large expansion in internal mélange areas observed in 2022 (Figure 2b).

Figure 4a shows that the smallest fracture bins (≤2 km and 2–4 km) exhibit an overall increasing trend with time. By contrast, the number of fractures exceeding 8 km in length remains almost the same over time. During phase 1 (2002 and 2006), the cumulative distribution function (CDF) curves indicated that medium-to-large-length fractures comprised a larger proportion of the shear-zone fractures. After 2006, the CDF curves exhibited a shift toward a higher proportion of smaller length fractures.

We also analyzed the changing orientation of these fractures using rose diagrams for 2002, 2006, 2010, 2014, 2018, and 2021 (Figure 4). Here we focused on two length categories: smaller fractures (≤4 km in length), which increase in number over time, and longer fractures (>8 km in length). Throughout the study period, long fractures maintained a relatively consistent orientation, predominantly between 105° and 120° clockwise from grid north (0° in EPSG:3031). Notably, the orientation of these long fractures became more consistently clustered at this angle after 2006 with minimal angular spread. Additionally, the count remains relatively constant over time, consistent with limited propagation or formation of new long fractures, despite downstream advection. By contrast, short fractures exhibited significant changes in their number and orientation, particularly after 2014. While earlier years (2002–2006) showed dominant orientations below 60°, later years (2018–2021) revealed broader angular distributions extending from 0° to 120°, with peaks shifting toward 60°–90°. This observation indicates that the short fracture distributions became roughly perpendicular to the long fractures.

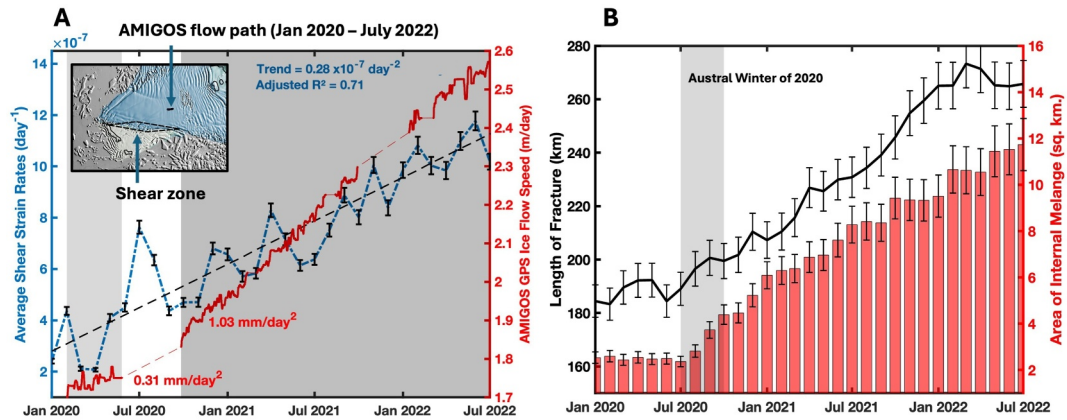

Figure 5. Monthly changes in fractures and shearing from January 2020 to July 2022. (a) Monthly time series of average shear strain rates across the shear zone within the pinning-point shear zone (blue dotted line) from Sentinel-1-derived velocities and mid-shelf ice-flow speed (red line) captured by AMIGOS GPS observation from January 2020 to July 2022. The light and dark gray patches show the two distinct periods with different accelerations when the data were available. The black dotted line shows the linear trend of shearing within this period. In the inset image, the black polygon shows the area where the time series of shear strain rates is calculated. (b) total length of the fractures and area of internal mélange for each month from January 2020 to July 2022. The gray patch in (b) illustrates the Austral winter months from July 2020 to October 2020, where significant growth of fracture and mélange was observed.

3.3. Evolution of Fractures and Dynamics in the Austral Winter of 2020

In situ GPS data allow a more detailed evaluation of dynamics during the rapid expansion of the mélange area from January 2020 to July 2022 (Figure 5a). Throughout this period, we identified a consistent mid-shelf acceleration with a noteworthy shift in velocity trend during the austral winter of 2020 (Figure 5a). The initial acceleration of 0.31 mm/d^2 from February to May 2020 increased to 1.03 mm/d^2 starting in October 2020. From March to October 2020, we had a large data gap in the AMIGOS record. However, we had uninterrupted records of Sentinel-1-derived velocity and surface strain rates at the monthly scale, enabling us to assess changes in dynamics within the shear zone for that duration. We reduced the spatial extent of the shear zone (Figure 5a inset) for this analysis as substantial data gaps emerged with the demise of Sentinel 1B after December 2021. Our monthly time-series record of shear strain rates, spatially averaged across the shear zone, demonstrates a consistent increasing trend at a rate of 0.28×10^{-7} day^{-2} (Figure 5a). A prominent increase was detected during the austral winter (July and August) of 2020, when the AMIGOS data were unavailable (Figure 5a). In tandem with these observations, the total fracture lengths and mélange areas also demonstrated an abrupt rise (Figure 5b) and continued to expand in the subsequent months.

During the Austral winter of 2020, we observed a sharp transition between slow- and fast-flowing ice within the shear zone, indicating a prominent line of localized shearing that we refer to as a line of maximum shearing (red dotted line in Figure 6a). The mélange expansion observed at this time originated from the western sector of the shelf, closely aligned with this line of maximum shearing, where an existing rift widened. During this time, the line of maximum shearing underwent a substantial shift upstream from August 2020 to October 2020 (as highlighted by the red dotted line and distinguishable from the velocity differences along the fractures in Figures 6a–6c).

To explore this dynamic change in detail, we consider velocity changes along two profiles targeting the evolving shearing signal at the western (DD') and central (EE') segments of the shelf while intersecting the AMIGOS flow path (Figure 6). We find a velocity perturbation emanating from the line of maximum shearing and propagating toward the mid-shelf ice with an average propagation speed of 55 ±10 km/yr, commencing in austral winter 2020. Particularly in the profile of DD', a prominent and strong shearing signal emerged in July 2020 that had not existed before (Figure 6: DD'). In addition, the ice flow upstream of the line of shearing exhibited a strong and progressive acceleration in the following months. These changes coincide with the location and time of the abrupt upstream shift in the line of shearing (Figures 6a–6c). In profile EE', three velocity bands can be observed, indicating the locations of the line of shearing where fractures have occurred. These features are indicated with arrows in the Hovmöller diagrams. In profile EE' (Figure 6), the rightmost shearing line also generates a strong

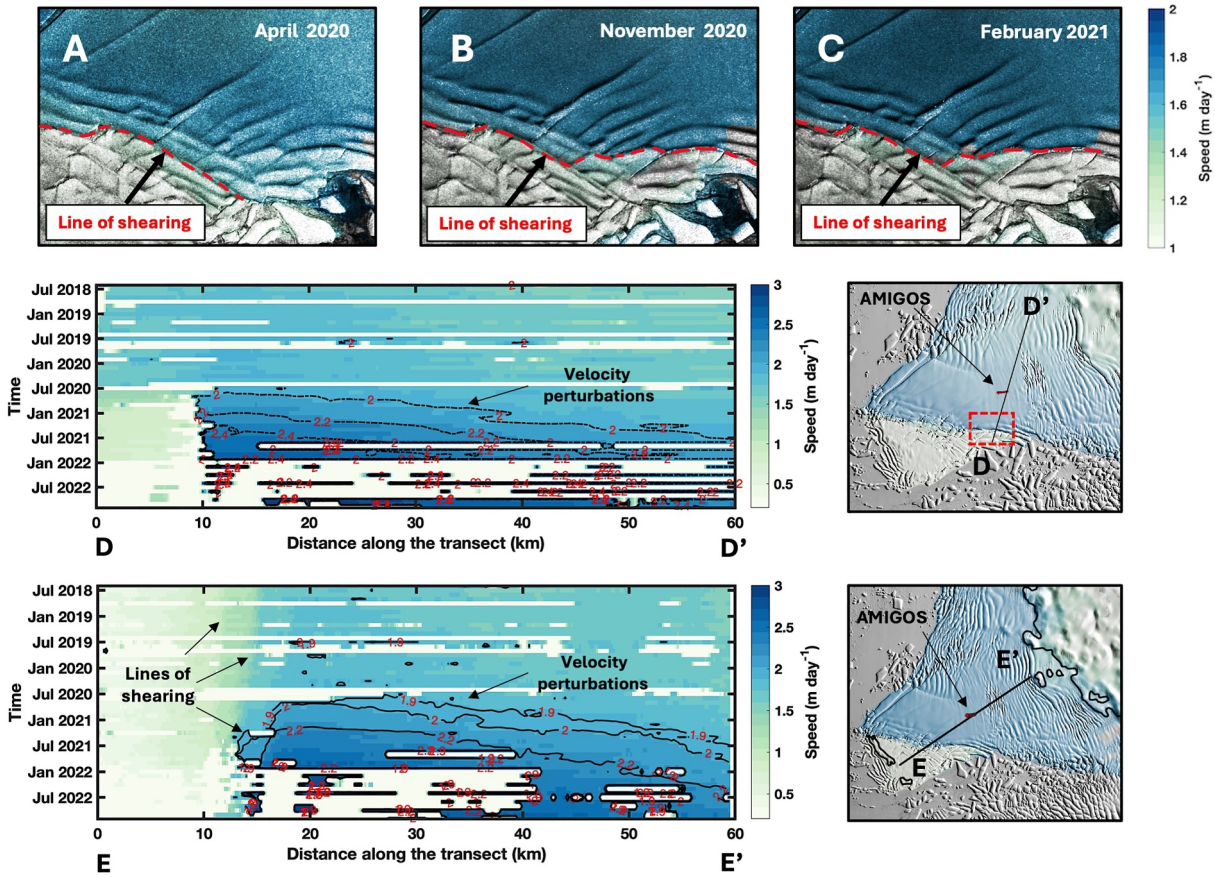

Figure 6. Relocation of the line of shearing during the Austral winter of 2020. (a–c) flow speed of Thwaites Eastern Ice Shelf (TEIS) overlaid on the fractures captured on Sentinel-1 images from April 2020, November 2020, and February 2021. The red dotted line marks the changing line of shearing on TEIS over these months. The lower panels show Hovmöller diagrams across two distinct profiles of TEIS along the western (DD'), central (EE') and parts of the shelf for capturing the signal of shearing. The location of these profiles is marked in the spatial map on the right side of the respective Hovmöller diagram. The background image in the spatial map is Landsat 9 for 2022. The red dotted rectangle shows the locations of (a–c) in TEIS. The black lines show contours of velocity (m/day) propagating from the western part of the shelf, closer to the line of shearing. In the profile EE', three prominent lines of shearing are mentioned in black dotted lines.

velocity perturbation. This line was also formed in July 2020 and corresponds to the same line of shearing observed in profile DD'. In contrast, the other two shearing lines in profile EE' predate this event and their locations coincide with the locations of the two long shear fractures. These older fractures are also evident in Figure 3a (2014 and 2016), where the shearing strain rate was the highest. The perturbation pattern in this profile also continues (similar to DD'), originating from the rightmost central shear line and exhibiting a lag time of about one to 2 months. The average propagation speed of the lines of shearing in both profiles is estimated to be approximately 0.75–1.1 km/yr, calculated from the slope in the Hovmöller diagrams.

4. Discussion

4.1. Chronology of Shear-Zone Fracture Evolution and a Two-Stage Fracture Development Process

We analyze the evolution of TEIS shear-zone fractures in response to changing flow dynamics (Figure S2 in Supporting Information S1) and the shelf's interaction with its pinning point and adjacent TWIT through four different phases. In phase 1 (2002–2006), the TWIT flow speed was nearly four times greater than that of TEIS, with a prominent shear margin separating the two entities (Alley, Wild, et al., 2021). During this period, the shear margin remained structurally intact (Alley, Wild, et al., 2021; Miles et al., 2020; Mouginot et al., 2014), which caused an acceleration of TEIS as it was dragged forward by TWIT. The peak velocity of TEIS was recorded around 2005–2006 (Alley, Wild, et al., 2021), and the highest acceleration during this phase was found in the mid-western segment of the mid-shelf region, proximal to the TEIS/TWIT shear margin (Figure 7a: 2002–2006). This

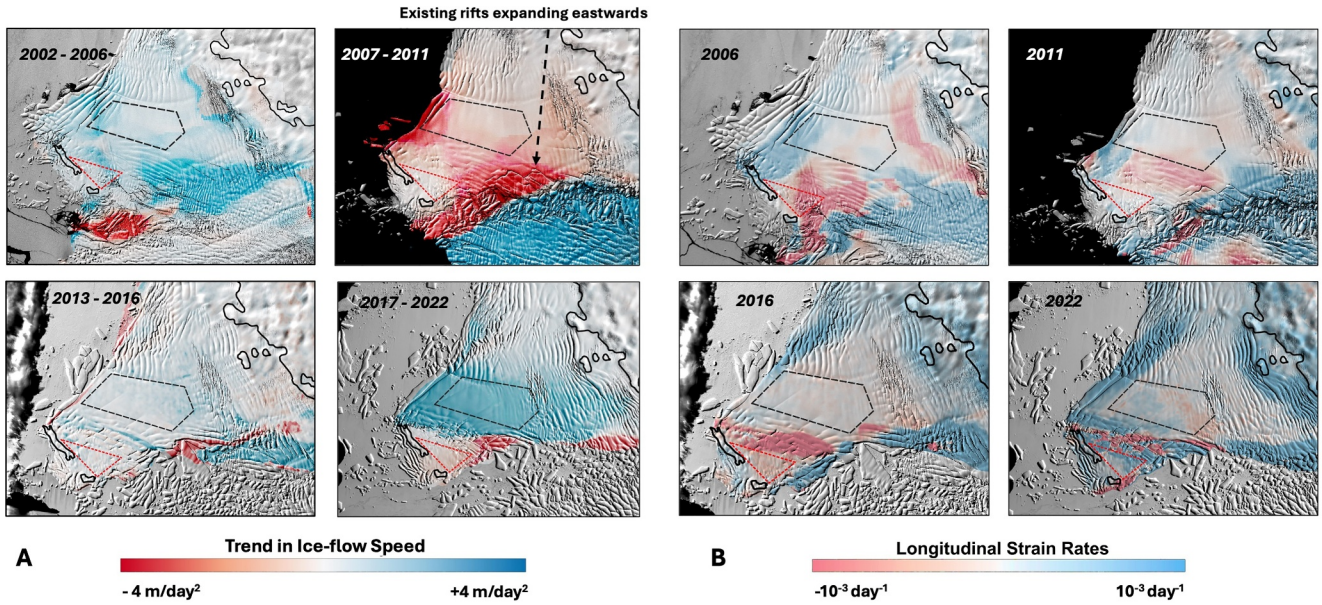

Figure 7. Trend in flow speed and longitudinal strain rates on Thwaites Eastern Ice Shelf (TEIS). (a) Trend in ice flow-speed of TEIS and Thwaites Western Ice Tongue (TWIT) during four different periods – 2002–2006 (Phase 1: TWIT-induced acceleration period), 2007–2011 (Phase 2: Shear margin disintegration), 2013–2016 (Phase 3: TWIT disintegration phase), and 2017–2022 (Phase 4: mid-shelf acceleration period). (b) Longitudinal strain rates over TEIS in 2006, 2011, 2016, and 2022 at the end of each period shown in (a). The trend in speed is calculated by fitting a linear model to the velocity time series at each pixel. It represents the rate of change in flow speed (m/yr^2) over the entire phase. The background images include Landsat-7 and 8 panchromatic band images for respective years. The black dashed polygon and the red dotted polygon delineate the location of the mid-shelf area and the region upstream of the pinning point, respectively, which are compared in Figure 8. Thwaites Glacier grounding lines for 2019/2020 from height above flotation (Wild et al., 2022) are used in each figure.

acceleration caused the mid-shelf region to experience intense longitudinal stretching. At the same time, the ice upstream of the pinning point underwent widespread compression in response to the basal resistance from the pinning point (Figure 7b: 2006 and Figure 8b: blue patch). Expansion of the large shear fractures within the pinning-point shear zone was prominent during this period. The dynamic drag from TWIT imparted a strong divergence of flow upstream of the pinning point, facilitating the ongoing concentration of strain and intensifying damage (Benn et al., 2022).

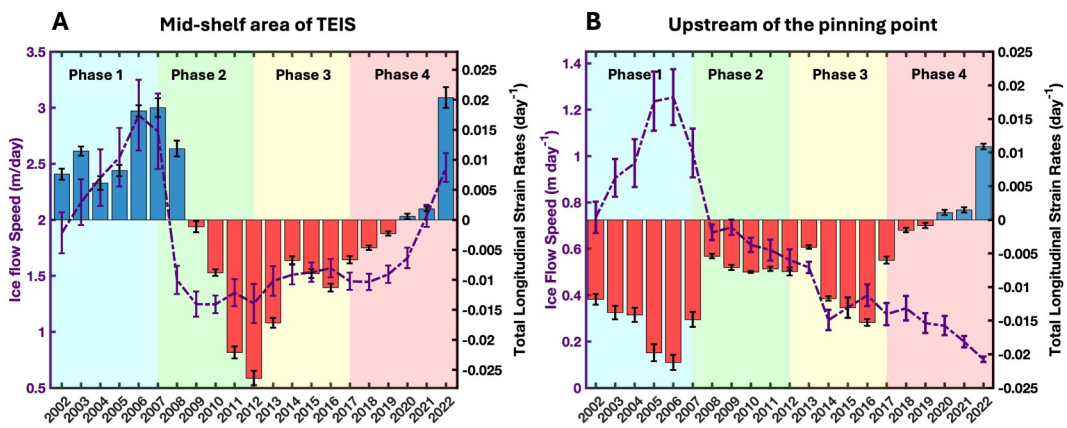

Figure 8. Time series of flow speed and longitudinal strain in two distinct areas on Thwaites Eastern Ice Shelf. Time series of average ice-flow speed (violet dotted line with standard error) and flow-oriented total longitudinal strain rates (red and blue bars with black dotted lines as standard error) over (a) mid-shelf region (upstream of the shear zone) and (b) upstream of the pinning point (downstream of the shear zone). The blue bars represent an extensional regime, and the red bars represent a compressive regime. Blue, green, yellow and red patches in the background represent Phases 1, 2, 3, and 4, respectively. Regions are shown in Figure 7.

In phase 2 (2007–2011), numerous rifts grew across the TEIS/TWIT shear margin, weakening the zone's integrity and culminating in its complete disintegration by 2008–2009 (Alley, Wild, et al., 2021). After the shear margin disintegration, TEIS decelerated. The maximum deceleration was found in the same location within the mid-western part of the shelf where the highest acceleration was observed during the earlier phase (Figure 7a: 2006–2011). Following the TEIS/TWIT shear-margin disintegration, some of the preexisting fractures along the shear margin continued to localize the shear strain and propagated eastward. Concurrently, a notable shift in the high compression band was observed from just upstream of the pinning point toward the fractures within the shear zone (Figure 7b: 2011). Also, the widespread compression observed in the earlier phase had substantially reduced as the shelf experienced reduced effects from the fast-flowing TWIT due to the shear-margin breakup (Figure 8b: green patch). The mid-shelf region also transformed into a compressive regime by 2008, which persisted for the next few years (Figure 8a: green patch).

During phase 3 (2012–2016), the overall flow speed of TEIS remained almost unchanged (Figure 7a: 2013–2016). However, from 2013 onwards, we observed the continued eastward propagation of long shear fractures, gradually expanding across the width of the ice shelf. The locations of these fractures were closely aligned with the bands of high shear strain rates (Figure 3a: 2014). Notably, these bands of high strain rates revealed the zones of structural weakness months before the subsequent fracture propagation became visible in the satellite imagery (also mentioned by Wild et al., 2024). Progressive expansion of the shear fractures started to compromise the shelf's structural integrity, slowly weakening its connection to its pinning point. As a result, the mid-shelf region began to experience a slow increase in speed. Subsequently, a population of small tensile cracks began to appear steadily across the shear zone. Their orientations were typically orthogonal to the direction of ice flow (Figure 4 and S2 in Supporting Information S1), indicating their tensile origin. Simultaneously, the band of high longitudinal compression migrated downstream, maintaining a consistent spatial alignment with the shear zone fractures (Figure 7b, 2016). Throughout this period, the total longitudinal strain rates remained compressive consistently across both the mid-shelf region and the area upstream of the pinning point (Figures 8a and 8b; yellow patches).

Phase 4 (2017–2022) began after the long shear fractures completely penetrated the entire width of the shelf, causing a nearly complete disconnection of the mid-shelf ice from its pinning point. Small tensile fractures exhibited a rapid and consistent growth in number within the shear zone, accompanied by the progressive elongation of several individual fractures. Their elongation was not confined to the shear zone boundary but also propagated upstream into the previously intact mid-shelf ice. One of the most prominent examples is the upstream propagation of five rifts from the shear zone since January 2016, as outlined in detail by Wild et al. (2024). Phase 4 was also characterized by a prominent segmentation of the shelf into two different flow regimes. Upstream of the shear zone, mid-shelf ice exhibited sustained acceleration with an eastward flow orientation, while the ice mass confined between the shear zone and the pinning point underwent deceleration (Figures 8a and 8b: red patch). The boundary between these two flow regimes coincided with a prominent line of shearing (Figure 7a: 2017–2022). As a result of the near-complete disconnection of the shelf with its pinning point, the resistance within the mid-shelf ice was manifested in shear rather than the compressive support earlier provided by the pinning point. In the following years, we observed a progressive decline in compressive strain within the mid shelf and a corresponding increase in longitudinal stretching (Figure 8a: red patch; Figure 7b: 2022). By 2020, this transition culminated in the transformation of the mid-shelf region from a compressive to an extensional stress regime (Figure 8a: red patch), which continued to persist and further strengthen until the end of the study period. At the same time, following the disconnection, resistance from the pinning point became increasingly confined to the ice mass between the pinning point and the shear zone. This region also exhibited fracturing in recent years (Figure 8b: red patch), ultimately transitioning to an extensional stress regime by 2020. This reduction in resistance is likely associated with the northward propagation of some of the tensile fractures from the shear zone toward the pinning point, as evidenced by localized patches of tensile strain in the ice upstream of the pinning point (Figure 7b: 2022).

The TEIS dynamics during Phase 4 (Figures 8a and 8b: red patch) illustrate a stark contrast to the dynamics in Phase 1 (blue patch). During Phase 1, the ice shelf maintained an extensional flow regime in the mid-shelf region, counterbalanced by a compressive regime upstream of the pinning point (Figure 8a). By Phase 4, the mid-shelf region again exhibited pronounced longitudinal stretching, but the area upstream of the pinning point entered an extensional regime (Figure 8b). This shift occurred due to the rapid development of shear-zone fractures upstream of the pinning point, which affected the flow dynamics and allowed the mid-shelf ice to deviate eastward after 2020, bypassing the mechanical resistance previously imposed by the pinning point. Overall, we identified a two-stage

fracture evolution process in the TEIS shear zone. The first stage was initiated by the eastward propagation of large shear fractures from the TEIS/TWIT shear margin that progressively weakened the mechanical connection between the shelf and its pinning point. These fractures substantially affected flow dynamics, which in turn initiated the second stage, marked by the onset of widespread dense tensile fracturing within the shear zone.

4.2. Shear-Zone Impacts on Upstream Ice-Shelf Dynamics

In the preceding sections, we highlighted how a rapid and consistent increase in fracturing within the shear zone, especially in phase 4, resulted in a loss of structural integrity, and progressively segmented the shelf into two distinct flow regimes after 2017. A prominent line of shearing demarcated the boundary between the accelerating mid-shelf and decelerating ice mass upstream of the pinning point. In addition, the AMIGOS GPS observations also revealed an acceleration of mid-shelf ice from January 2020 to July 2022, with a particularly sharp rise in trend (+0.66 mm/d^2) observed in the austral winter of 2020 (March to October), as noted by Scambos et al. (2025). We found that this substantial rise in mid-shelf flow velocity occurred when the line of maximum shearing exhibited an upstream shift around the western flank of the TEIS due to new fracture propagation. As a result, we observed strong velocity perturbations propagating upstream from the shear zone across the ice shelf (Figure 6). The origination of these patterns at the observed line of maximum shearing suggests that the loss of structural integrity around the shear zone had a significant impact on the upstream mid-shelf acceleration. This also demonstrates that the pinning point has provided some ongoing support to the rest of TEIS at least until 2022 despite extensive shear-zone fracturing.

Benn et al. (2022) described a self-reinforcing feedback mechanism between damage concentration and strain localization within the TEIS shear zone that has contributed to progressive weakening of the ice shelf. Lhermitte et al. (2020) also illustrated a comparable feedback process through numerical experiments on a synthetic ice shelf, showing how initial damage and strain concentration can amplify localized weakening along shear margins, resulting in upstream acceleration, which in turn induces more shearing and damage. Although our analysis does not include modeling to establish the existence of such a feedback between damage, strain, and upstream flow acceleration in TEIS, some of our observations suggest a resemblance with the early stages of this mechanism (also mentioned by Wang et al. (2025)). First, we observed a strong temporal correlation between upstream acceleration, shear strain localization, and structural weakening during the terminal years of our study period (Figures 2c and 5). Second, the velocity perturbations emanating from the shear zone (Figure 6) and propagating across the mid-shelf indicate that the shear-zone disintegration has a strong influence on the upstream flow dynamics. These changes became quite pronounced after 2017, likely following the propagation of rifts that nearly disconnected the mid-shelf from its pinning point. Our observations are therefore consistent with the existence of a positive feedback between damage and flow acceleration as described by Benn et al. (2022) and Lhermitte et al. (2020). This interpretation also highlights the need for future studies employing targeted numerical modeling experiments to test the presence, strength, and evolution of this mechanism. Further intensification of this feedback mechanism might exacerbate dynamic thinning, fracturing, and calving, and it is reasonable to suspect that this feedback will play an important role during the final stages of TEIS's life.

4.3. Implications

Shear margins are susceptible to large-scale fracturing where strain rates and stresses are high, often exceeding thresholds for mechanical failure (Alley et al., 2019; Schulson, 2001). Our analysis provides observations on the sequence of fracturing processes at the TEIS shear zone, offering a benchmark for future modeling efforts. We document a two-stage fracture evolution process: an initial phase dominated by the propagation of long, shearing rifts, followed by a transition to more spatially dense tensile fracturing. The sequence offers insight into the progressively intensifying mechanical failure around a shear zone under evolving stress conditions, which may also be relevant across other Antarctic ice shelves. In addition, we show that fracture evolution within the shear zone is not an isolated structural response but is dynamically linked to upstream ice flow (Matsuoka et al., 2015; Miele et al., 2023). At TEIS, we observed velocity perturbations propagating from the close vicinity of the shear zone across the mid-shelf, indicating that localized fracturing near the pinning point can modulate the upstream dynamics of the shelf. Finally, the acceleration in upstream flow might lead to further strain concentration, and more localized weakening, a process that may also operate in other Antarctic ice shelves exhibiting complex dynamic interactions with their pinning points.

Benn et al. (2022) highlighted the transforming role of the TEIS pinning point from a stabilizing agent to a destabilizing agent for an ice shelf. Our study provides a detailed documentation of how that transition happened in different phases through changes in internal stress conditions, fracturing, and flow dynamics. In the initial years, compressive resistance from the pinning point provided structural support and stability to the shelf. Over time, changing dynamic interaction with TWIT and sustained shearing against the pinning point emerged as a dominant destabilizing driver, contributing to rapid disintegration of the ice shelf. A comparable mechanism appears to underlie the observations from Doake and Vaughan (1991) on the changing role of Buffer Ice Rise, from stabilizing the Wordie Ice Shelf to facilitating its eventual decoupling. In the early 1970s, compression against the Buffer ice rise stabilized the Wordie Ice Shelf. However, with ice-front retreat, the ice rise became a nucleation point for rifts, eventually causing decoupling of the shelf from its pinning point. A similar pattern has also been found on the Conger-Glenzer ice shelf, where the evolution of rifts has significantly weakened the ice shelf's connection with its pinning points (Walker et al., 2024), although it was the extreme weather events that triggered the final collapse of the shelf. Notably, in TEIS's case, the role of its dynamic interaction with its neighboring TWIT for the last two decades cannot be ignored. Stress transmission between TWIT and TEIS likely accelerated the disintegration of TEIS against its pinning point, a process not shared by many other ice shelves.

The location of an ice shelf also plays a crucial role in determining the interaction of external drivers, such as the atmospheric and oceanic conditions, in regulating the ice shelf processes. TEIS is located in the Amundsen Sea Embayment region, where ocean-driven basal melting has been recognized as a key external factor contributing to the thinning and weakening of the ice shelves (Davis et al., 2023; Wåhlin et al., 2021; Wild et al., 2022). Observations by Davis et al. (2023) indicate that modest basal melt rates have been associated with the rapid retreat rate of the grounding line beneath TEIS since 2011. A remotely sensed estimation by Adusumilli et al. (2020) indicates a mean basal melt rate of 1.05 ± 0.71 m a^{-1} beneath the Eastern Ice Shelf from 1994 to 2018, while more recent in situ records indicate a median melting rate of 1.07 ± 1.02 m a^{-1} between December 2019 and January 2020 (Wild et al., 2024). Despite these observed trends, the extent to which basal melting intensity and duration have varied within the shear zone—and how these variations may have contributed to fracturing—remains uncertain. It is plausible that sustained basal melting might have preconditioned the shear zone ice by reducing its thickness and making it more susceptible to breaking (Benn et al., 2022; Clark et al., 2024; Wåhlin et al., 2021) under sustained stresses. However, given the relatively modest melt rates observed in recent years, basal melt alone appears insufficient to drive the current pace of shear-zone disintegration. Notably, Wild et al. (2024) reported that the ongoing propagation rate of rifts across central TEIS outpaces the rate of basal melting, which suggests that the final stage of ice-shelf destabilization is largely driven by dynamic processes rather than direct melt-induced weakening.

Our findings elucidate how TEIS's dynamic interaction with its pinning point and neighboring TWIT over the last two decades has gradually compromised the shelf's structural integrity, thereby affecting the pinning-point buttressing the grounded ice upstream. Our results show that the pinning point has provided some continuing support to the ice shelf, with velocity perturbations emanating from the shear zone discernible since 2020. Modeling experiments by Gudmundsson et al. (2023) suggest that the ice shelf in its current state provides limited buttressing to the Thwaites Glacier, and that its complete removal will have no discernible effect on the future mass loss. Wild et al. (2024) reported the opening and widening of rift "gashes" near the grounding line, which implies that TEIS has detached from the glacier and no longer transmits much buttressing to the grounded ice. The locations of these "gashes" have been found consistent with the regions where we observed acceleration accompanied by intense longitudinal stretching in recent years. However, recent work suggests that the remaining buttressing provided by the ice shelf has shifted to small embayments along its complex grounding zone (Wang et al., 2025). In addition, the presence of the ice shelf might have an indirect impact on preventing the overturning, calving, or evacuation of icebergs, and continued breakup of the ice shelf might still have important effects on the Thwaites Glacier (Wild et al., 2024). In short, while we show that TEIS provides less buttressing than in the past, consistent with past work, TEIS may still exert dynamic control on ice upstream.

5. Conclusion

Benn et al. (2022) demonstrated how the TEIS pinning point transitioned from a stabilizing feature to a destabilizing agent. Our study investigates how this transition has unfolded over the past two decades. We demonstrate how the "compression against the pinning point," once the major stabilizing force, has gradually transformed into "shearing against the pinning point," a source of fracture and a major destabilizing driver for the shelf in recent

times. We document a comprehensive chronology of TEIS over the past two decades and explain the fracture evolution pattern within the pinning-point shear zone in relation to the changing flow dynamics and the shelf's mechanical interaction with its pinning point and neighboring TWIT in four different phases.

We identified a two-stage fracture process occurring within the TEIS shear zone. The onset of fracturing within the TEIS shear zone was linked to the shelf's dynamic interaction with TWIT during the earlier years of the study period. After TEIS/TWIT shear-margin disintegration, some of the existing fractures from the disintegrated shear-margin localized the shear strain concentration and facilitated an eastward propagation in the subsequent years. As these fractures gradually penetrated across the shelf's width, they disrupted the mechanical connection between the ice shelf and its pinning point. Consequently, this disruption affected the shelf's dynamics in the subsequent years. The mid-shelf flow gradually reoriented eastward with flow acceleration. Simultaneously, numerous small tensile fractures began to proliferate within the shear zone, further exacerbating the damage. Their orientation was typically orthogonal to the flow direction. This two-stage process of fracturing—initiating with the expansion of large shear fractures followed by dynamics-driven dense tensile fracturing—might also be seen in other pinning-point shear zone disintegrations. Although we recognize the fact that the interactions between TWIT and TEIS had placed a substantial amount of stress on this pinning point, which might not have analog elsewhere.

Our findings demonstrate that the progressive disintegration of the shear zone exerts a dynamic influence on the upstream flow. During the terminal phase of TEIS's evolution, we detect a coherent pattern of velocity perturbations emanating from the shear zone and propagating across the mid-shelf domain, suggesting a strong dynamic linkage between localized structural failure and its shelf-wide flow response. In addition, we have seen accelerated mid-shelf flow correlating with increasing shear strain rates and fracture growth within the shear zone, particularly after 2017, after the long shear zone fractures nearly disconnected the shelf from its pinning point. We find that the sequence of events observed during the terminal phase of TEIS is consistent with the initiation phase of a self-reinforcing feedback mechanism, as proposed by Lhermitte et al. (2020). This mechanism involves damage accumulation within shear margins, localizing strain concentration and promoting upstream acceleration, which in turn exacerbates damage further. If this feedback is operating on TEIS, it is likely to accelerate its disintegration.

Data Availability Statement

The digitized fractures and internal mélange areas from the Landsat and Sentinel-1 images are available from Banerjee et al. (2025a) at the U.S. Antarctic Program Data Center. The Landsat scenes are freely available from the USGS Earth Explorer (https://earthexplorer.usgs.gov/), and Sentinel-1 images can be downloaded from the Copernicus Open Access Hub (https://scihub.copernicus.eu/). The NASA ITS_LIVE ice-flow velocity image pairs are freely available from https://its-live.jpl.nasa.gov/, and the ITS_LIVE processed annual composites (120 m resolution) used in this study from 2013 to 2022 can be obtained Banerjee et al. (2025b). The MODIS-derived Two-year velocity and strain-rate average composites can be downloaded from Alley, Klinger, et al. (2021). The monthly flow velocity derived from Sentinel-1 can be available from Banerjee et al. (2025c). The processed AMIGOS GPS data can be obtained from Truffer et al. (2025).

Acknowledgments
This research was undertaken, in part, thanks to funding from the Canada Excellence Research Chairs Program to Dr. Dorthe Dahl-Jensen. Additional financial support was provided from the University of Manitoba Graduate Fellowship (UMGF). We are also grateful for the support from the entire community of the Centre for Earth Observation Science (CEOS) at the University of Manitoba. This work was supported by Natural Sciences and Engineering Research Council of Canada (NSERC) RGPIN-2021-02910 and NSF OPP-1738992, the Thwaites-Amundsen Regional Survey and Network (TARSAN) Project of the International Thwaites Glacier Collaboration (ITGC). This work is published under the TARSAN project, a component of the International Thwaites Glacier Collaboration, ITGC Contribution No. ITGC-150. Support is received from the National Science Foundation (NSF: Grant 1929991) and the Natural Environment Research Council (NERC: Grant NE/S006419/1). Logistics provided by NSF-U.S. Antarctic Program and NERC-British Antarctic Survey. We thank the two anonymous reviewers for their constructive feedback and suggestions.

References

Adusumilli, S., Fricker, H. A., Medley, B., Padman, L., & Siegfried, M. R. (2020). Interannual variations in meltwater input to the Southern Ocean from Antarctic ice shelves. *Nature Geoscience*, *13*(9), 616–620. https://doi.org/10.1038/s41561-020-0616-z

Alley, K. E., Klinger, M., Muto, A., Pettit, E. C., Scambos, T., Truffer, M., et al. (2021). Two-year velocity and strain-rate averages from the Thwaites eastern ice shelf, 2001-2020 [Dataset]. *U.S. Antarctic Program (USAP) Data Center*. https://doi.org/10.15784/601478

Alley, K. E., Alley, R. B., Crawford, A. D., Ochwat, N., Wild, C. T., Marson, J., et al. (2024). Evolution of sub-ice-shelf channels reveals changes in ocean-driven melt in West Antarctica. *Journal of Glaciology*, *70*, e50. https://doi.org/10.1017/jog.2024.20

Alley, K. E., Scambos, T. A., Alley, R. B., & Holschuh, N. (2019). Troughs developed in ice-stream shear margins precondition ice shelves for ocean-driven breakup. *Science Advances*, *5*(10), eaax2215. https://doi.org/10.1126/sciadv.aax2215

Alley, K. E., Scambos, T. A., Anderson, R. S., Rajaram, H., Pope, A., & Haran, T. M. (2018). Continent-wide estimates of Antarctic strain rates from Landsat 8-derived velocity grids. *Journal of Glaciology*, *64*(244), 321–332. https://doi.org/10.1017/jog.2018.23

Alley, K. E., Wild, C. T., Luckman, A., Scambos, T. A., Truffer, M., Pettit, E. C., et al. (2021). Two decades of dynamic change and progressive destabilization on the Thwaites Eastern Ice Shelf. *The Cryosphere*, *15*(11), 5187–5203. https://doi.org/10.5194/tc-15-5187-2021

Banerjee, D., Alley, K., Lilien, D., Luckman, A., Muto, A., Pettit, E. C., et al. (2025a). Pinning-point shear-zone fractures in Thwaites eastern ice shelf (2002 - 2022) [Dataset]. *U.S. Antarctic Program (USAP) Data Center*. https://doi.org/10.15784/601903

Banerjee, D., Alley, K., Lilien, D., Luckman, A., Muto, A., Pettit, E. C., et al. (2025b). Yearly velocity and strain-rate averages from the Thwaites eastern ice shelf, 2013-2022 [Dataset]. *U.S. Antarctic Program (USAP) Data Center*. https://doi.org/10.15784/601904

Banerjee, D., Alley, K., Lilien, D., Luckman, A., Muto, A., Pettit, E. C., et al. (2025c). Sentinel-1-derived monthly-averaged velocity components from Thwaites eastern ice shelf, 2016–2022 [Dataset]. *U.S. Antarctic Program (USAP) Data Center*. https://www.usap-dc.org/view/dataset/601914

Benn, D. I., Luckman, A., Åström, J. A., Crawford, A. J., Cornford, S. L., Bevan, S. L., et al. (2022). Rapid fragmentation of Thwaites eastern ice shelf. *The Cryosphere*, *16*(6), 2545–2564. https://doi.org/10.5194/tc-16-2545-2022

Clark, R. W., Wellner, J. S., Hillenbrand, C. D., Totten, R. L., Smith, J. A., Miller, L. E., et al. (2024). Synchronous retreat of Thwaites and Pine Island glaciers in response to external forcings in the presatellite era. *Proceedings of the National Academy of Sciences*, *121*(11), e2211711120. https://doi.org/10.1073/pnas.2211711120

Davis, P. E. D., Nicholls, K. W., Holland, D. M., Schmidt, B. E., Washam, P., Riverman, K. L., et al. (2023). Suppressed basal melting in the eastern Thwaites Glacier grounding zone. *Nature*, *614*(7948), 479–485. https://doi.org/10.1038/s41586-022-05586-0

Doake, C. S. M., & Vaughan, D. G. (1991). Rapid disintegration of the Wordie Ice Shelf in response to atmospheric warming. *Nature*, *350*(6316), 328–330. https://doi.org/10.1038/350328a0

Dotto, T. S., Heywood, K. J., Hall, R. A., Scambos, T. A., Zheng, Y., Nakayama, Y., et al. (2022). Ocean variability beneath Thwaites eastern ice shelf driven by the pine Island Bay Gyre strength. *Nature Communications*, *13*(1), 7840. https://doi.org/10.1038/s41467-022-35499-5

Fahnestock, M., Scambos, T., Moon, T., Gardner, A., Haran, T., & Klinger, M. (2016). Rapid large-area mapping of ice flow using Landsat 8. *Remote Sensing of Environment*, *185*, 84–94. https://doi.org/10.1016/j.rse.2015.11.023

Fretwell, P., Pritchard, H. D., Vaughan, D. G., Bamber, J. L., Barrand, N. E., Bell, R., et al. (2013). Bedmap2: Improved ice bed, surface and thickness datasets for Antarctica. *The Cryosphere*, *7*(1), 375–393. https://doi.org/10.5194/tc-7-375-2013

Gardner, A. S., Fahnestock, M. A., & Scambos, T. A. (2019). *ITS_LIVE regional glacier and ice sheet surface velocities* (Vol. 10). Data Archived at National Snow and Ice Data Center. Retrieved from https://scholar.google.com/scholar?cluster=7693506252152797194&hl=en&oi=scholarr

Gudmundsson, G. H., Barnes, J. M., Goldberg, D. N., & Morlighem, M. (2023). Limited impact of Thwaites ice shelf on future ice loss from Antarctica. *Geophysical Research Letters*, *50*(11), e2023GL102880. https://doi.org/10.1029/2023GL102880

Herring, T., King, R., & Mcclusky, S. (2008). Introduction to GAMIT.

Hill, E. A., Urruty, B., Reese, R., Garbe, J., Gagliardini, O., Durand, G., et al. (2023). The stability of present-day Antarctic grounding lines – Part 1: No indication of marine ice sheet instability in the current geometry. *The Cryosphere*, *17*(9), 3739–3759. https://doi.org/10.5194/tc-17-3739-2023

Howat, I. M., Porter, C., Smith, B. E., Noh, M.-J., & Morin, P. (2019). The reference elevation model of Antarctica. *The Cryosphere*, *13*(2), 665–674. https://doi.org/10.5194/tc-13-665-2019

Joughin, I., Smith, B. E., & Medley, B. (2014). Marine ice sheet collapse potentially under way for the Thwaites Glacier basin, west Antarctica. *Science*, *344*(6185), 735–738. https://doi.org/10.1126/science.1249055

Lei, Y., Gardner, A., & Agram, P. (2021). Autonomous repeat image feature tracking (autoRIFT) and its application for tracking ice displacement. *Remote Sensing*, *13*(4), 749. https://doi.org/10.3390/rs13040749

Lhermitte, S., Sun, S., Shuman, C., Wouters, B., Pattyn, F., Wuite, J., et al. (2020). Damage accelerates ice shelf instability and mass loss in Amundsen Sea Embayment. *Proceedings of the National Academy of Sciences*, *117*(40), 24735–24741. https://doi.org/10.1073/pnas.1912890117

Luckman, A., Benn, D. I., Cottier, F., Bevan, S., Nilsen, F., & Inall, M. (2015). Calving rates at tidewater glaciers vary strongly with ocean temperature. *Nature Communications*, *6*(1), 8566. https://doi.org/10.1038/ncomms9566

Matsuoka, K., Hindmarsh, R. C., Moholdt, G., Bentley, M. J., Pritchard, H. D., Brown, J., et al. (2015). Antarctic ice rises and rumples: Their properties and significance for ice-sheet dynamics and evolution. *Earth-Science Reviews*, *150*, 724–745. https://doi.org/10.1016/j.earscirev.2015.09.004

Miele, C., Bartholomaus, T. C., & Enderlin, E. M. (2023). Marginal detachment zones: The fracture factories of ice shelves? *Journal of Geophysical Research: Earth Surface*, *128*(6), e2022JF006959. https://doi.org/10.1029/2022JF006959

Miles, B. W. J., Stokes, C. R., Jenkins, A., Jordan, J. R., Jamieson, S. S. R., & Gudmundsson, G. H. (2020). Intermittent structural weakening and acceleration of the Thwaites Glacier tongue between 2000 and 2018. *Journal of Glaciology*, *66*(257), 485–495. https://doi.org/10.1017/jog.2020.20

Milillo, P., Rignot, E., Rizzoli, P., Scheuchl, B., Mouginot, J., Bueso-Bello, J. L., et al. (2022). Rapid glacier retreat rates observed in West Antarctica. *Nature Geoscience*, *15*(1), 48–53. https://doi.org/10.1038/s41561-021-00877-z

Morlighem, M., Rignot, E., Binder, T., Blankenship, D., Drews, R., Eagles, G., et al. (2020). Deep glacial troughs and stabilizing ridges unveiled beneath the margins of the Antarctic ice sheet. *Nature Geoscience*, *13*(2), 132–137. https://doi.org/10.1038/s41561-019-0510-8

Mouginot, J., Rignot, E., & Scheuchl, B. (2014). Sustained increase in ice discharge from the Amundsen Sea Embayment, west Antarctica, from 1973 to 2013. *Geophysical Research Letters*, *41*(5), 1576–1584. https://doi.org/10.1002/2013GL059069

Nye, J. F. (1959). A method of determining the strain-rate tensor at the surface of a glacier. *Journal of Glaciology*, *3*(25), 409–419. https://doi.org/10.3189/S0022143000017093

Reese, R., Garbe, J., Hill, E. A., Urruty, B., Naughten, K. A., Gagliardini, O., et al. (2023). The stability of present-day Antarctic grounding lines – Part 2: Onset of irreversible retreat of Amundsen Sea glaciers under current climate on centennial timescales cannot be excluded. *The Cryosphere*, *17*(9), 3761–3783. https://doi.org/10.5194/tc-17-3761-2023

Rignot, E., Mouginot, J., Morlighem, M., Seroussi, H., & Scheuchl, B. (2014). Widespread, rapid grounding line retreat of pine Island, Thwaites, Smith, and Kohler glaciers, west Antarctica, from 1992 to 2011. *Geophysical Research Letters*, *41*(10), 3502–3509. https://doi.org/10.1002/2014GL060140

Rignot, E., Mouginot, J., Scheuchl, B., van den Broeke, M., van Wessem, M. J., & Morlighem, M. (2019). Four decades of Antarctic ice sheet mass balance from 1979–2017. *Proceedings of the National Academy of Sciences*, *116*(4), 1095–1103. https://doi.org/10.1073/pnas.1812883116

Scambos, T. A., Bell, R. E., Alley, R. B., Anandakrishnan, S., Bromwich, D. H., Brunt, K., et al. (2017). How much, how fast? A science review and outlook for research on the instability of Antarctica's Thwaites Glacier in the 21st century. *Global and Planetary Change*, *153*, 16–34. https://doi.org/10.1016/j.gloplacha.2017.04.008

Scambos, T. A., Ross, R., Haran, T., Bauer, R., Ainley, D. G., Seo, K.-W., et al. (2013). A camera and multisensor automated station design for polar physical and biological systems monitoring: Amigos. *Journal of Glaciology*, *59*(214), 303–314. https://doi.org/10.3189/2013JoG12J170

Scambos, T. A., White, T., Wallin, B., Truffer, M., Collao-Barrios, G., Kratt, C., et al. (2025). AMIGOS-3 multi-sensor stations and the climate, ice, and ocean conditions at Thwaites Eastern Ice Shelf during 2020-2022. *Journal of Glaciology*, 1–38. https://doi.org/10.1017/jog.2024.96

Schmidt, B. E., Washam, P., Davis, P. E. D., Nicholls, K. W., Holland, D. M., Lawrence, J. D., et al. (2023). Heterogeneous melting near the Thwaites Glacier grounding line. *Nature*, *614*(7948), 471–478. https://doi.org/10.1038/s41586-022-05691-0

Schoof, C. (2007a). Ice sheet grounding line dynamics: Steady states, stability, and hysteresis. *Journal of Geophysical Research*, *112*(F3), L00G07. https://doi.org/10.1029/2006jf000664

Schoof, C. (2007b). Marine ice-sheet dynamics. Part 1. The case of rapid sliding. *Journal of Fluid Mechanics*, *573*, 27–55. https://doi.org/10.1017/S0022112006003570

Schulson, E. M. (2001). Brittle failure of ice. *Engineering Fracture Mechanics*, *68*(17), 1839–1887. https://doi.org/10.1016/S0013-7944(01)00037-6

Seabold, S., & Perktold, J. (2010). Statsmodels: Econometric and statistical modeling with python. *SciPy*, *7*(1), 92–96. https://doi.org/10.25080/Majora-92bf1922-011

Seroussi, H., Nakayama, Y., Larour, E., Menemenlis, D., Morlighem, M., Rignot, E., & Khazendar, A. (2017). Continued retreat of Thwaites Glacier, West Antarctica, controlled by bed topography and ocean circulation. *Geophysical Research Letters*, *44*(12), 6191–6199. https://doi.org/10.1002/2017GL072910

Truffer, M., Alley, K., Pettit, E. C., Scambos, T., & Wild, C. (2025). *Thwaites eastern ice shelf GPS displacements*. U.S. Antarctic Program (USAP) Data Center. https://doi.org/10.15784/601925

Virtanen, P., Gommers, R., Oliphant, T. E., Haberland, M., Reddy, T., Cournapeau, D., et al. (2020). SciPy 1.0: Fundamental algorithms for scientific computing in Python. *Nature Methods*, *17*(3), 261–272. https://doi.org/10.1038/s41592-019-0686-2

Wåhlin, A. K., Graham, A. G. C., Hogan, K. A., Queste, B. Y., Boehme, L., Larter, R. D., et al. (2021). Pathways and modification of warm water flowing beneath Thwaites ice shelf, west Antarctica. *Science Advances*, *7*(15), eabd7254. https://doi.org/10.1126/sciadv.abd7254

Walker, C. C., Millstein, J. D., Miles, B. W., Cook, S., Fraser, A. D., Colliander, A., et al. (2024). Multi-decadal collapse of east Antarctica's Conger–Glenzer ice shelf. *Nature Geoscience*, *17*(12), 1240–1248. https://doi.org/10.1038/s41561-024-01582-3

Wang, S., Alexander, P. M., Alley, R. B., Huang, Z., Parizek, B. R., Willet, A. G., & Anandakrishnan, S. (2025). Recent variability in fracture characteristics and ice flow of Thwaites ice shelf, west Antarctica. *Journal of Geophysical Research: Earth Surface*, *130*(5), e2024JF008118. https://doi.org/10.1029/2024JF008118

Whitaker, J., Snow, A. D., Cochran, M., Karney, C., Ouzounoudis, G., Dearing, J., et al. (2019). Jswhit/pyproj: Version 2.0.2 release. *Zenodo*. https://doi.org/10.5281/zenodo.2592233

Wild, C. T., Alley, K. E., Muto, A., Truffer, M., Scambos, T. A., & Pettit, E. C. (2022). Weakening of the pinning point buttressing Thwaites Glacier, west Antarctica. *The Cryosphere*, *16*(2), 397–417. https://doi.org/10.5194/tc-16-397-2022

Wild, C. T., Kachuck, S. B., Luckman, A., Alley, K. E., Sharp, M. A., Smith, H., et al. (2024). Rift propagation signals the last act of the Thwaites Eastern Ice Shelf despite low basal melt rates. *Journal of Glaciology*, *70*, 1–18. https://doi.org/10.1017/jog.2024.64

Wolfe, R. E., Nishihama, M., Fleig, A. J., Kuyper, J. A., Roy, D. P., Storey, J. C., & Patt, F. S. (2002). Achieving sub-pixel geolocation accuracy in support of MODIS land science. *Remote Sensing of Environment*, *83*(1), 31–49. https://doi.org/10.1016/S0034-4257(02)00085-8